Final Report for AOARD Grant FA2386-11-1-4114
"Growth of GaN Nanorods and Their Coalescence Overgrowth"

September 7, 2012

Name of Principal Investigators: Chih-Chung (C. C.) Yang
- e-mail address : ccy@cc.ee.ntu.edu.tw
- Institution : Graduate Institute of Photonics and Optoelectronics, National Taiwan University
- Mailing Address : No. 1, Roosevelt Road, Section 4, Taipei, 10617 Taiwan
- Phone : +886-2-23657624
- Fax : +886-2-23652637

Period of Performance: 10/01/2011 – 09/30/2012

Abstract:

With the nano-imprint lithography and the pulsed growth mode of metalorganic chemical vapor deposition, a regularly-patterned, c-axis nitride nanorod (NR) array of quite uniform geometry with simultaneous depositions of top-face, c-plane disc-like and sidewall, m-plane core-shell InGaN/GaN quantum well (QW) structures is formed. The differences of geometry and composition between these two groups of QW are studied with scanning electron microscopy, cathodoluminescence, and transmission electron microscopy (TEM). In particular, the strain state analysis results in TEM observations provide us with the information about the QW width and composition. It is found that the QW widths are narrower and the indium contents are higher in the sidewall m-plane QWs, when compared with the top-face c-plane QWs. Also, in the sidewall m-plane QWs, the QW width (indium content) decreases (increases) with the height on the sidewall. The observed results can be interpreted with the migration behaviors of the constituent atoms along the NR sidewall from the bottom. Besides, we demonstrate the growth of a conducting nitride layer of low vertical resistance (64 Ω) on 6H n-type SiC substrate. The nitride layer consists of a 150-nm n-AlGaN layer with the Al composition being linearly decreased from 20 to 0 % and a 1-μm n-GaN layer. Both layers are Si doped with a level around 10^{18}/cm^3. The growth condition of the n-AlGaN layer must be further improved to obtain a crack-free and smooth surface.

Table of Contents:

Report Documentation Page		*Form Approved* *OMB No. 0704-0188*

Public reporting burden for the collection of information is estimated to average 1 hour per response, including the time for reviewing instructions, searching existing data sources, gathering and maintaining the data needed, and completing and reviewing the collection of information. Send comments regarding this burden estimate or any other aspect of this collection of information, including suggestions for reducing this burden, to Washington Headquarters Services, Directorate for Information Operations and Reports, 1215 Jefferson Davis Highway, Suite 1204, Arlington VA 22202-4302. Respondents should be aware that notwithstanding any other provision of law, no person shall be subject to a penalty for failing to comply with a collection of information if it does not display a currently valid OMB control number.

1. REPORT DATE **07 SEP 2012**	2. REPORT TYPE **Final**	3. DATES COVERED **14-09-2011 to 13-09-2012**
4. TITLE AND SUBTITLE **Growth of Gallium Nitride Nanorods and Their Coalescence Overgrowth**		5a. CONTRACT NUMBER **FA23861114114**
		5b. GRANT NUMBER
		5c. PROGRAM ELEMENT NUMBER
6. AUTHOR(S) **Chih-Chung Yang**		5d. PROJECT NUMBER
		5e. TASK NUMBER
		5f. WORK UNIT NUMBER
7. PERFORMING ORGANIZATION NAME(S) AND ADDRESS(ES) **National Taiwan University,Institute of Electro-Optical Engineering, Room 445,Taipei 10617,Taiwan,TW,10617**		8. PERFORMING ORGANIZATION REPORT NUMBER **N/A**
9. SPONSORING/MONITORING AGENCY NAME(S) AND ADDRESS(ES) **AOARD, UNIT 45002, APO, AP, 96338-5002**		10. SPONSOR/MONITOR'S ACRONYM(S) **AOARD**
		11. SPONSOR/MONITOR'S REPORT NUMBER(S) **AOARD-114114**

12. DISTRIBUTION/AVAILABILITY STATEMENT
Approved for public release; distribution unlimited

13. SUPPLEMENTARY NOTES

14. ABSTRACT
With the nano-imprint lithography and the pulsed growth mode of metalorganic chemical vapor deposition, a regularly-patterned, c-axis nitride nanorod (NR) array of quite uniform geometry with simultaneous depositions of top-face, c-plane disc-like and sidewall, m-plane core-shell InGaN/GaN quantum well (QW) structures is formed. The differences of geometry and composition between these two groups of QW are studied with scanning electron microscopy, cathodoluminescence, and transmission electron microscopy (TEM). In particular, the strain state analysis results in TEM observations provide us with the information about the QW width and composition. It is found that the QW widths are narrower and the indium contents are higher in the sidewall m-plane QWs, when compared with the top-face c-plane QWs. Also, in the sidewall m-plane QWs, the QW width (indium content) decreases (increases) with the height on the sidewall. The observed results can be interpreted with the migration behaviors of the constituent atoms along the NR sidewall from the bottom. Besides, we demonstrate the growth of a conducting nitride layer of low vertical resistance (64 Ω) on 6H n-type SiC substrate. The nitride layer consists of a 150-nm n-AlGaN layer with the Al composition being linearly decreased from 20 to 0 % and a 1-μm n-GaN layer. Both layers are Si doped with a level around 1018/cm3. The growth condition of the n-AlGaN layer must be further improved to obtain a crack-free and smooth surface.

15. SUBJECT TERMS
Gallium Nitride , nano materials, Detector Technology, Electronic Devices, Coalescence Overgrowth, Threading Dislocations

16. SECURITY CLASSIFICATION OF:			17. LIMITATION OF ABSTRACT	18. NUMBER OF PAGES	19a. NAME OF RESPONSIBLE PERSON
a. REPORT **unclassified**	b. ABSTRACT **unclassified**	c. THIS PAGE **unclassified**	**Same as Report (SAR)**	**22**	

Part I:
InGaN/GaN Quantum-well Nanorod Arrays

1. Introduction

Growth of nitride nanorods (NRs) (or called nanowires, nanocolumns, or nanoposts) for light-emitting diode (LED) application has several advantages. First, in an NR, threading dislocation density can be reduced [1, 2]. When the NR cross-sectional dimension is smaller than a few hundred nm, threading dislocation can be completely eliminated [1]. Therefore, the crystal quality of a nitride NR can be higher than that of a planar structure. Second, due to its small dimension, the lateral strain relaxation in an NR on either top-face [3, 4] or sidewall plane can occur to result in higher indium incorporation for high-indium InGaN growth [5]. Third, the sidewall or core-shell growth of a c-axis-oriented NR can lead to non-polar quantum well (QW) growth [6, 7] for eliminating the quantum-confined Stark effect (QCSE) in a QW structure [8, 9]. Also, the growth on the slant {1-101} facets at the pyramidal top of an NR can lead to the formation of semi-polar QWs for reducing the QCSE [10, 11]. Fourth, due to the three-dimensional structure of an NR array, the emission area of an arrayed NR LED can be larger than that of a planar LED structure [6, 7, 12]. For instance, in a triangular-patterned NR array of 600 nm in the height of the sidewall, 440 nm in the distance between two parallel lateral sides of a hexagonal NR cross section, and 700 nm in the nearest center-to-center NR separation, if the NR sidewalls are fully covered by InGaN/GaN QWs, the total sidewall emission area is about 1.86 times the area of a planar LED structure. An array of higher NRs will lead to an even larger enhancement factor in emission area. Fifth, strong light scattering by the NR surfaces in an NR LED array can enhance light extraction efficiency [4, 13]. Meanwhile, a proper arrangement of the NR pattern can lead to controlled radiation angle dependence [13]. Sixth, GaN NR growth and coalescence overgrowth can result in a GaN thin film of significantly improved crystal quality [1, 14]. Such a high-quality GaN thin film can be used as the template for the growth of a high-efficiency LED [15]. With the residual NR structure beneath, the laser liftoff of sapphire substrate in such an epitaxial structure for vertical LED fabrication becomes easier. Finally, by growing GaN NRs on silicon substrate, thermal stress can be released such that wafer cracking can be avoided and the crystal quality of the coalesced overgrown layer can be improved [16].

Randomly-distributed self-organized GaN NRs have been widely grown on sapphire and silicon substrates with molecular beam epitaxy (MBE) and metalorganic chemical vapor deposition (MOCVD). In the self-organized growth, GaN NRs can be grown from certain nucleation centers in an AlN or SiN$_x$ buffer layer. In this situation, the planar locations of NRs and their cross-sectional dimensions and heights are randomly distributed. With MBE growth, the orientations of self-organized NRs are essentially mutually parallel and vertical to the substrate [17, 18]. Usually, self-organized GaN NRs can be grown with MBE under the nitrogen-rich condition when the growth temperature is high (roughly >750 ^{o}C). Self-organized GaN NRs can also be grown with MOCVD based on the vapor-liquid-solid (VLS) growth mode either with catalyst or without catalyst [19, 20]. Without an extrinsic catalyst, gallium can be used as the self-catalyst in the VLS

growth mode. However, with MOCVD growth, usually the self-organized GaN NRs are randomly oriented. Although self-organized GaN NRs have provided us with quite many physical insights, their application is limited due to their non-uniform distribution of geometry and hence their non-uniform distributions of optical and electronic properties. Selected or patterned growths of GaN NRs have also widely been implemented with MBE [21, 22] and MOCVD [1, 14, 23]. The regularly patterning methods include electron-beam writing [21], focused ion beam [22], holography [23], and nano-imprint [1, 14]. In regularly patterned growth, vertically oriented NRs of uniform size and height distributions can be obtained. With MOCVD growth, the pulsed growth mode, in which the gallium and nitrogen sources are switched on and off alternatively, is usually used for implementing the self-catalyst VLS growth mode [1, 14, 23].

For LED application, InGaN/GaN QW p-i-n NR structures have been widely reported. On a *c*-axis GaN NR, InGaN/GaN QWs can be classified into the following three categories. First, on the flat top face of an NR, a disc-like *c*-plane (polar) QW structure can be formed. In this situation, the NR top can eventually become a pyramidal geometry. Second, on the slant {1-101} facets of the top pyramid geometry of an NR, semi-polar QWs can be grown. Third, on the sidewalls of an NR, a core-shell *m*-plane QW structure can be formed. Disc-like QWs have been widely grown with MBE [22, 24-26]. The growth of slant-facet QWs on the {1-101} sixfold side-facets of the pyramidal top of an NR with MBE has also been reported [10]. With selected-area MOCVD growth, most efforts led to the growth of a pyramid structure, on which QWs were formed on the slant {1-101} facets and a quantum dot could be formed at the tip [27-30]. N-polarity GaN NRs were fabricated on *c*-plane sapphire substrate with MOCVD [31]. On such an NR, QWs were grown on the flat and slant facets at the top [11]. On the other hand, with MOCVD, core-shell QWs and hetero-structures have been grown on *a*-axis-oriented GaN NRs [12, 32, 33]. Recently, *m*-plane QWs on the sidewalls of *c*-axis-oriented N-polarity GaN NRs were successfully grown and a single-NR LED based on such a growth has been fabricated [6, 34, 35]. However, their QWs were formed only in a certain sidewall range near the top. Also, the positions and geometries of the grown NRs were randomly distributed. For implementing an NR LED array, regularly patterned NRs of uniform geometry are required. The fabrication of a regularly patterned NR LED array with top-face and sidewall InGaN/GaN quantum structures for tuning the emission color in the visible range was recently reported [7]. However, in their work, by depositing the quantum structures on the GaN NRs of truncated pyramidal tops, InGaN layers of unclear quantum structures and crystal facets were formed in the NRs. Also, the large variation of emission wavelength in changing the applied voltage indicates the significantly non-uniform indium-content distribution along the height of an NR. No informative characterization results of the quantum structures in their NRs were reported.

In this part of the report, the pulsed MOCVD growth and characterization of a regularly patterned, c-axis-oriented nitride NR array of Ga-polarity on sapphire substrate with c-plane InGaN/GaN QWs on the NR flat-top face and m-plane QWs on the NR sidewalls are reported. The NR geometry, QW structures, and emission characteristics are studied with scanning electron microscopy (SEM), cathodoluminescence (CL), and transmission electron microscopy (TEM). In

particular, the strain state analysis (SSA) technique is applied to analyze the QW widths and indium compositions at different locations on an NR. It is found that the QW widths are narrower and the indium compositions are higher in the sidewall m-plane QWs, when compared with the top-face c-plane QWs. Also, in the sidewall m-plane QWs, the QW width (indium composition) decreases (increases) with the height on the sidewall. In section 2 of this part of report, the fabrication procedures for the QW NR array are presented. Also, the characterization methods, including the principle and operation of SSA, are reported in section 2. Then, the SEM and CL measurement results are discussed in section 3. The TEM observation results are given in section 4. Next, the SSA results are provided in section 5. Discussions are made in section 6. Finally, the conclusions are drawn in section 7.

2. Nanorod growth and characterization conditions

The NR growth is patterned with the nano-imprint technique on a 2-μm-thick GaN template, which is deposited with MOCVD on c-plane sapphire substrate [1, 14]. On the wafer, a two-dimensional (2-D) triangular pattern of circular holes of 250 nm in diameter and 700 nm in the nearest center-to-center separation is formed on a 40-nm-thick SiO_2 mask. The growth of GaN NRs starts with a hole-filling process under the MOCVD conditions of 100 torr in chamber pressure, 1500 rpm in turbo disc speed, 1050 ^{o}C in substrate temperature, 50 sccm in TMGa flow rate, 1500 sccm in NH3 flow rate (1100 in V/III ratio), and 12 sec in growth duration. After the hole filling process, the pulsed MOCVD growth mode is used at 1050 ^{o}C with V/III ratio at 550 for forming flat-top GaN NRs [1, 14, 23]. In this process, TMGa (50 sccm) and NH_3 (500 sccm) flows are switched on and off alternatively with the flow durations of TMGa and NH_3 at 20 and 30 sec, respectively. A pause of 0.5 sec in duration is applied after each TMGa flow cycle. After the pulsed growth for ~20 min (25 cycles), regularly patterned GaN NRs of uniform geometry with a height of ~600 nm are obtained. On the GaN NRs, three periods of InGaN/GaN QWs are deposited with the conventional 2-D MOCVD growth mode under the conditions of 200 torr in chamber pressure, 750 rpm in turbo disc speed, 32 sccm in TEGa flow rate, 2700 sccm in NH3 flow rate, and 240 sccm in TMIn flow rate (only applied to the growth of the InGaN well layers). The growth temperature and duration of the InGaN well (GaN barrier) in the QW structures are 700 ^{o}C and 1.25 min (870 ^{o}C and 11 min), respectively. The SEM measurement is performed with a JEOL JSM-7001F system, in which a Gatan MonoCL4 module is installed for CL measurement. The SEM (CL) results are obtained with the operation conditions of 10 kV (5 kV) in acceleration voltage and 0.3 nA (7 nA) in probe current. The spatial resolution of SEM is ~3 nm and that of CL is ~10 nm. A local CL spectral measurement covers a spatial domain of 100 x 75 nm^2 in dimension. The TEM investigation is performed using a Philips Tecnai F30 field-emission electron microscope with an accelerating voltage of 300 kV and a probe forming lens of Cs = 1.2 mm. The high-resolution micrographs for SSA are taken with two-electron-beam interference. The current density focused onto the sample is estimated to be lower than 16 A/cm^2. With the two-beam interference data, the SSA for obtaining composition distributions can be performed [36]. To obtain an SSA image, the lattice size distribution is first calibrated from the lattice fringe image. The lattice size distribution is represented by a parameter, d, defined as the ratio of the local lattice size over that of GaN. Then,

the indium composition distribution can be calibrated based on Vegard's law subject to a control factor. This factor is related to the thickness of the TEM specimen [36]. However, it is usually difficult to determine such a thickness. In our analysis, we use the indium content of a previously-grown planar InGaN/GaN QW sample of surely determined indium composition at ~7 % as the reference for calibrating the data of the sample under study based on the variation of the parameter d [37, 38]. The indium content of 7 % corresponds to the value of d at 1.033. Based on this correspondence, we can estimate the thickness of our TEM specimen as around 50 nm, which is quite reasonable. Therefore, the local indium composition can be obtained by using the formula of 212 % x (d – 1) [36-38].

3. Results of scanning electron microscopy and cathodoluminescence

Figures 1(a) and 1(b) show the plan-view and 30°-tilted SEM images, respectively, of the GaN NR array before the deposition of InGaN/GaN QWs. In Fig. 1(a), one can see that the hexagonal shapes of some of the GaN NRs are slightly asymmetric. The degree of symmetry in the hexagonal cross section of an NR relies on the shape of the hole for NR growth. The distance between two parallel lateral sides in the hexagon of the central NR in Fig. 1(a), as indicated by the arrow, is 376 nm. From Fig. 1(b), one can see that the tops of the GaN NRs are flat. The heights of the NRs are around 600 nm. After the deposition of three InGaN/GaN QWs, the plan-view and 30°-tilted SEM images of the NR array are shown in Figs. 1(c) and 1(d), respectively. In Fig. 1(c), one can see that the cross-sectional sizes of the QW NRs become larger. As indicated by the arrow in Fig. 1(c), the distance between two parallel lateral sides in the hexagon of the indicated NR is 452 nm. Then, in Fig. 1(d), one can see that the tops of the QW NRs become pointed with pyramidal shapes. The NR heights become slightly larger.
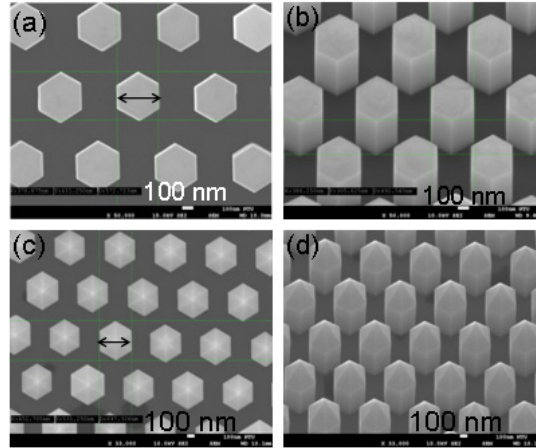

Fig. 1 Plan-view (a) and 30°-tilted (b) SEM images of the GaN NR array; Plan-view (c) and 30°-tilted (d) SEM images of the QW NR array.

Figures 2(a) and 2(b) show a plan-view SEM image and its corresponding panchromatic CL image, respectively, of the QW NR array. In the CL image, one can see the strong emission at the rim of each NR. CL emission also comes from the central portion of an NR in Fig. 2(b) although it is weaker. To differentiate the

emission characteristics at the rim and the central portion of the top of an NR, we measure the local CL spectra at the two locations indicated by the two rectangles in Fig. 2(a). The spectra measured at the center and rim of the NR top face are shown as curves TF-c and TF-r, respectively, in Fig. 3. For comparison, the large-scale plan-view CL spectrum (curve PV) is also shown in Fig. 3. Here, one can see that the three spectra are all peaked around 450 nm although the peak of curve TF-r is slightly red shifted. Figures 2(c) and 2(d) show a cross-sectional SEM image and its corresponding panchromatic CL image, respectively, of the QW NR array. Here, we can see that the CL emission intensity on the sidewall of an NR is quite uniform. To understand the different emission characteristics at different heights of the sidewall of an NR, we measure the local CL spectra at the three different sidewall locations near the top, middle height, and bottom, as indicated by the three rectangles in Fig. 2(c), to give the spectral curves labeled by SW-t, SW-m, and SW-b, respectively, in Fig. 3. Again, for comparison, the large-scale cross-sectional CL spectrum is also plotted as curve CS in Fig. 3. Here, one can see that the spectral peak wavelength red-shifts with height on the sidewall. The red-shift trend indicates that the QW geometry and composition may vary along the height of the sidewall on an NR. The large-scale cross-sectional CL spectrum covers the three spectra at different sidewall heights. In Fig. 3, we also plot the plan-view CL spectrum of the bare GaN NR array as the curve labeled by "PV-GaN" for reference. Here, one can see the GaN band-edge emission in the UV range and the broadband yellow luminescence from the defects. Such defect emissions can be strongly excited by the high-energy electrons in CL measurement.

4. Results of transmission electron microscopy

Figure 4(a) shows the cross-sectional TEM image of a QW NR. Here, we can clearly see three c-plane QWs at the NR top. Three m-plane QWs on the two sidewalls can also be observed although they are not very clear. The upper portion of Fig. 4(a) is magnified to give Fig. 4(b). Here, the three c-plane QWs can be more clearly seen. Meanwhile, at the lower ends of the two (1-101) planes, the sidewall QWs can be seen, as indicated by the arrows. The dark thick lines (broken at certain locations) at the rim of the NR correspond to the coated Pt layer during TEM specimen preparation with focused ion beam. The high angle annular dark field (HAADF) image of the top NR portion is shown in Fig. 4(c). In this image, one can see that among the three top-face QWs, the contrast of the bottom one is low, implying that its geometry is not well defined. It is noted that between the top c-plane QWs and the sidewall m-plane QWs, no clear InGaN quantum structure can be observed. This observation is better supported by the magnified image in Fig. 4(d). In other words, the widely reported {1-101}-plane QWs are not formed in our sample. Figures 4(e)-4(g) show the magnified TEM images of the sidewall QWs near the top, middle height, and bottom on either side of the NR. Here, one can clearly see that the QW spacing decreases with the height of the sidewall although it is difficult to read the QW widths. As shown in Fig. 4(g), at the NR bottom, the QWs bend following the original shape of GaN NR. In growing GaN NRs, at the rim of a circular hole on a template, GaN out-reaches on the SiO_2 mask to form a triangular bump [1].

Figure 5(a) shows the cross-sectional TEM image of a few fallen QW NRs. We focus the observation at the circled NR, whose image is magnified to give Fig. 5(b).

It is noted that those NRs contacted each other after they fell. Here, one can clearly see the three sidewall QWs on each lateral side of the hexagon, as indicated by arrows. The hexagon is quite asymmetric. The HAADF image (the left-side right) of the NR cross section is shown in Fig. 5(c), in which the notations A-F are assigned to represent the six lateral sides. The clear QW mapping in this figure allows us to measure the QW separations and lengths on each lateral side. To compare the QW separations and lengths among the six lateral sides, we define the geometric parameters in Fig. 5(d), in which a trapezium is plotted to represent the QW region on each lateral side. Here, the three thick dark (blue) lines stand for the three QWs with their lengths being defined as L_1, L_2, and L_3. The base of the trapezium is denoted by L_4. The separations between the QWs and the trapezium base are denoted by t_1, t_2, and t_3. The measured values of those geometric parameters for the lateral sides A-F are listed in rows 2-8 of Table I.
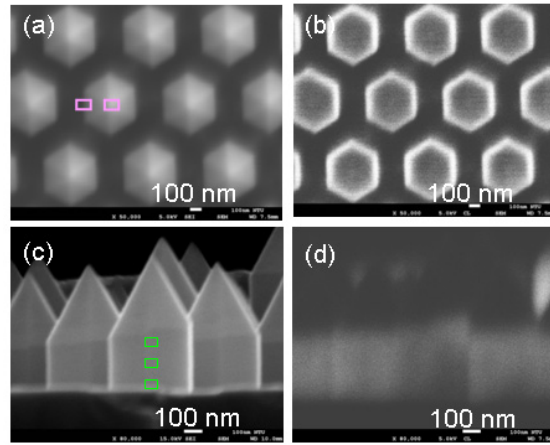

Fig. 2 Plan-view SEM (a) and the co-located panchromatic CL (b) images of the QW NR array; Cross-sectional SEM (c) and the co-located panchromatic CL (d) images of the QW NR array. The rectangles in parts (a) and (c) indicate the locations of local CL spectrum measurements.
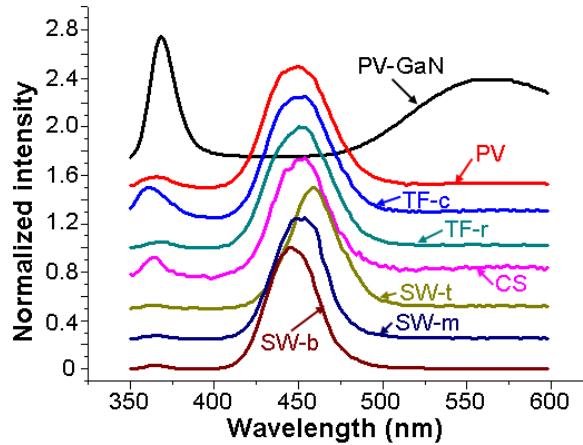

Fig. 3 CL spectra of the QW NR array measured at different locations and different view directions, including that from the large-scale plan-view (PV) measurement, that at the center on the top face of an NR (TF-c) and that at the rim on the top face of the NR (TF-r), that from the large-scale cross-sectional view (CS) measurement, that at a point near the top of the sidewall of an NR (SW-t), near the middle height of the sidewall of the NR (SW-m), and near the bottom of the sidewall of the

7

In Table I, on each lateral side, one can see the increasing trend from L_1 through L_4 and decreasing trend from t_1 through t_3. Among the six lateral sides, generally a larger QW length (L_x value, x = 1-4) corresponds to a smaller QW separation (t_x value, x = 1-3). It is noted that because we cannot determine the QW thicknesses at this stage, the QW separations are defined as the distances between the centers of two neighboring QWs. As to be shown in the next section, the sidewall QW widths are in the range of 1-2 nm. Therefore, the definition for the QW separation here represents a good approximation. If we use the lower two QWs to divide the large trapezium in Fig. 5(d) into three small trapeziums, we can evaluate the areas of the small trapeziums to give the results in rows 9-11 of Table I. The average of these three areas on each lateral side is listed in the bottom row of Table I. Also, on each lateral side, the deviation percentages of the areas of the small trapeziums from the average value are shown within the parentheses in the corresponding rows. Here, one can see that all the deviation percentages are smaller than 8.6 %. The roughly equal areas of the small trapeziums on each lateral side indicate the generally constant supply of GaN constituent atoms for each lateral side. Therefore, a larger lateral-side length corresponds to a smaller QW separation. The variations of the average area value in the bottom row of Table I can be regarded as the different supply quantities of GaN constituent atoms among the six lateral sides. Here, one can see that the lateral-sides D and F have significantly larger side lengths and also larger average areas, when compared with other lateral sides. Such results are reasonable since a lateral side of a larger side length is expected to adsorb more GaN constituent atoms. However, although lateral-side E has a significantly smaller side length, when compared with those of lateral-sides A and B, its average trapezium area is comparable to those of A and B. This result can be related to its protruding geometry for more effectively adsorbing the constituent atoms. The significantly smaller average trapezium area on lateral-side C, even though its side length is not small, can be attributed to the strong adsorption efficiency of its neighboring NRs or the non-uniform spatial distribution of supplied constituent atoms. Nevertheless, it is difficult to give an assured explanation.

Table I Measured QW geometric parameter values on the six lateral sides of the cross-sectional hexagon of a QW NR.

Lateral side	A	B	C	D	E	F
L_1 (nm)	219.4	213.4	198.8	296.1	148.8	266.1
t_1 (nm)	13.6	14.3	12.5	13.3	19.5	15.8
L_2 (nm)	230.9	232.6	219.5	313.1	159.1	283.7
t_2 (nm)	12.9	12.5	10.5	11.9	18.5	12.7
L_3 (nm)	242.7	246.3	237.5	329.6	165.6	307.8
t_3 (nm)	12.5	11.3	9.5	11.4	18.3	12.2
L_4 (nm)	256.5	257.2	249.7	342.9	175.8	333.4
$(L_1 + L_2)$ x t_1 /2 (nm^2)	3062.0 (-0.55%)	3188.9 (5.98%)	2614.4 (7.03%)	4051.2 (3.80%)	3002.0 (-1.35%)	4343.4 (8.52%)
$(L_2 + L_3)$ x t_2 /2 (nm^2)	3054.7 (-0.79%)	2993.1 (-0.53%)	2399.3 (-1.78%)	3824.1 (-2.02%)	3003.5 (-1.30%)	3756.0 (-6.16%)

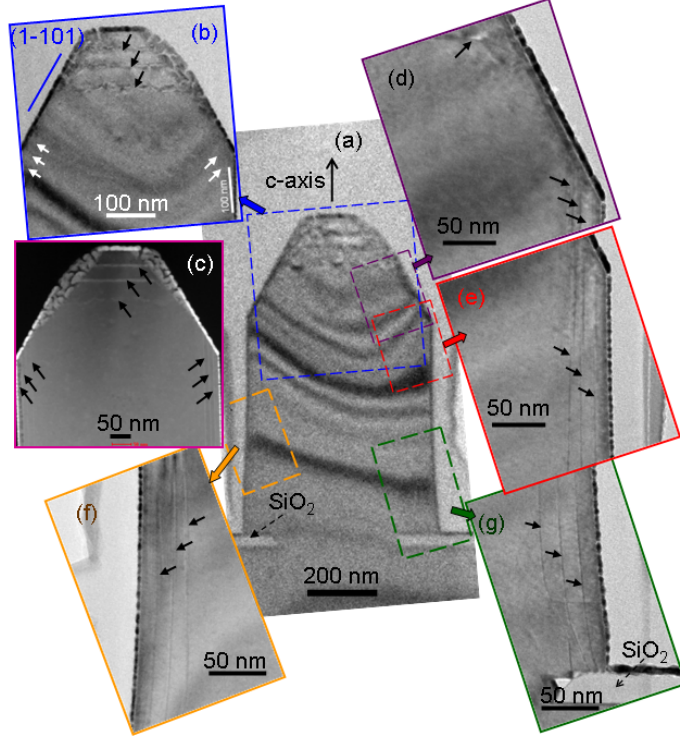| (L$_3$ + L$_4$) x t$_3$ /2 (nm^2)	3120.0 (1.33%)	2844.8 (-5.46%)	2314.2 (-5.26%)	3833.3 (-1.78%)	3123.8 (2.65%)	3908.1 (-2.36%)
Average (nm^2)	3078.9	3008.9	2442.6	3902.8	3043.1	4002.5

Fig. 4 (a) Cross-sectional TEM image of a QW NR. The portions of the top, the slant (1-101) facet on the right, the top sidewall on the right, the middle-height sidewall on the left, and the bottom sidewall on the right of the NR are magnified to show parts (b) and (d)-(g), respectively. The HAADF image of the NR top portion is shown in part (c).
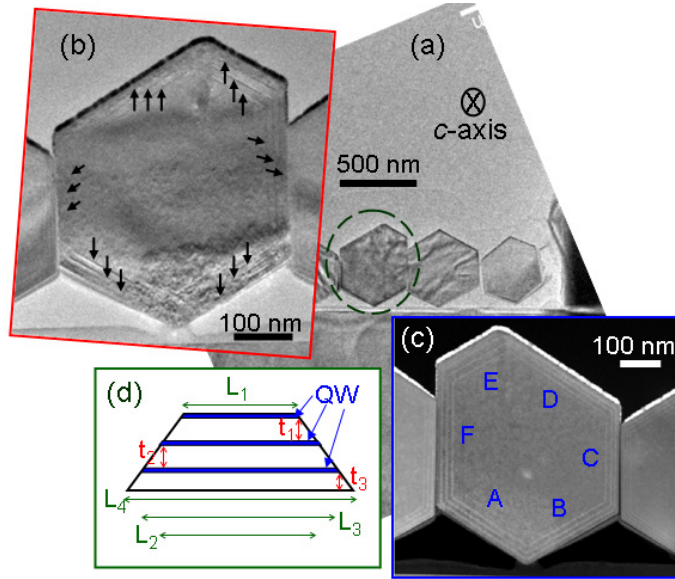

Fig. 5 (a) TEM image of a few fallen QW NRs; (b) The magnified TEM image of the QW NR circled in part (a), in which the three QWs on each lateral side of the hexagon are indicated by arrows. (c) The

9

HAADF version of the same TEM image in part (b), which has been imaged left-side right. The six lateral sides of the hexagon are designated as A-F. (d) Schematic drawing of the QW portion on a lateral side of the hexagon, in which the thick dark (blue) lines represent the three QWs. The separations between the QWs and surface are designated as t_1-t_3. The lateral lengths at different growth stages are designated as L_1-L_4.

5. Results of strain state analysis

To further study the geometries and compositions of the top-face and sidewall QWs, the SSA technique is used based on the two-beam TEM observation. Figures 6-9 show the SSA results of the typical QWs on the top face, near the top, middle height, and bottom on a sidewall, respectively. In each figure, part (a) shows the two-beam TEM image and part (b) illustrates the corresponding SSA image. It is normally difficult to find the direct correspondence between the two images. Then, part (c) in each figure demonstrates the line-scan SSA signal intensity profile along the vertical dashed line plotted in part (b). The color coding at the bottom of each figure shows the level of indium content. In Fig. 6, the spacing between two neighboring horizontal grid lines corresponds to one-half the local lattice size along the c-axis (~0.259 nm). In Figs. 7-9, that corresponds to the period of the m-planes, which is equal to the local lattice size along the a axis multiplied by $\sqrt{3}/2$ (~0.276 nm). In all the figures, the vertical grid lines are plotted to have the same local spacing as that in another dimension for reference [37]. The dimension of an SSA image is usually smaller than the corresponding two-beam TEM image because the SSA technique cannot be applied to an area containing a stacking fault. In Figs. 6-9, one can see that indium atoms out-diffuse from the designated QW areas. Also, a sidewall QW does not necessarily follow a straight line. Meanwhile, indium-rich nano-clusters exist in every QW [39]. With the out-diffused indium distributions in the QWs, it becomes difficult to directly read the QW widths. In our analysis, we evaluate the full-width at half-maximum (FWHM) of the indium content distribution in every vertical line scan of an SSA image as long as a clear single-peak profile can be observed. The QW width is defined as the average of the FWHMs over all the vertical line scans of clear single-peak profiles. After we evaluate the QW width, we can divide the total indium content in each SSA image by the evaluated QW width to obtain the average indium content of the QW. The total indium content in an SSA image can be obtained by simply integrating the indium content in each pixel of the whole image. The obtained indium content can be slightly underestimated because certain incorporated indium atoms may diffuse out of the SSA image. However, such a slight underestimation should not affect our discussions and conclusions in this study.

In Fig. 6(b) for a typical c-plane QW section on the top face, one can see that the indium distribution is poorly confined. The evaluated QW width and average indium content are 4.80 nm and 11.77 %, respectively. In Fig. 7(b) for a typical sidewall QW section near the top, one can see a quite well-confined indium distribution. The evaluated QW width and average indium content are 1.25 nm and 19.75 %, respectively. Then, in Fig. 8(b) for a typical sidewall QW section near the middle height, the indium out-diffusion becomes stronger, when compared that in Fig. 7(b). The evaluated QW width and average indium content are 1.36 nm and 18.38 %, respectively. Next, in Fig. 9(b) for a typical sidewall QW section near the bottom, the indium out-diffusion becomes even stronger. The evaluated QW width and average

indium content are 2.00 nm and 16.88 %, respectively. From the comparisons between the evaluation results in Figs. 6-9, one can see that the top-face QW has a significantly larger QW width and a lower indium composition, when compared with the sidewall QWs. At different heights, the width (indium composition) of the sidewall QW is the largest (lowest) near the NR bottom, followed by that around the middle height. However, a single image of one QW section may not be enough for determining the variation trends of the QW width and composition. For more reliable variation trends, we prepare five similar SSA images for each QW category to evaluate the average values. The average results of the QW width and indium content are shown in the second and third columns, respectively, of Table II. It is noted that the average values here are not accurate enough for representing the real QW widths and indium contents. However, their variation trends provide us with important information about the top-face and sidewall QW growths. In Table II, one can see that the top-face QWs indeed have a significantly larger average QW width at 4.72 nm, when compared with the sidewall QWs. Also, they have smaller average indium content. On the sidewall, the average QW width (indium content) decreases (increases) with the height on the sidewall.
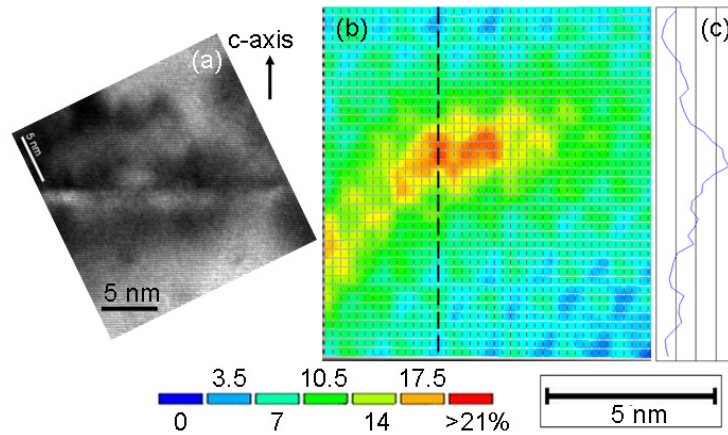

Fig. 6 Two-beam TEM image (a) and the corresponding SSA image (b) of a section of a top-face QW. Part (c) shows the line-scan indium content profile along the vertical dashed line in part (b).
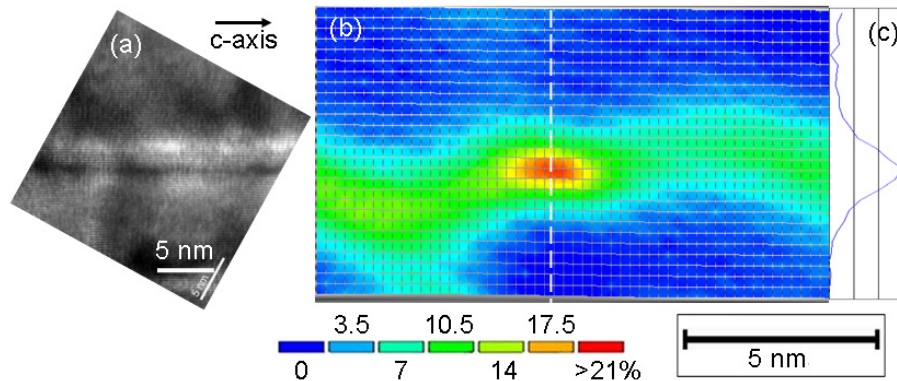

Fig. 7 Two-beam TEM image (a) and the corresponding SSA image (b) of a section of a sidewall QW near the top of the QW NR. Part (c) shows the line-scan indium content profile along the vertical dashed line in part (b).
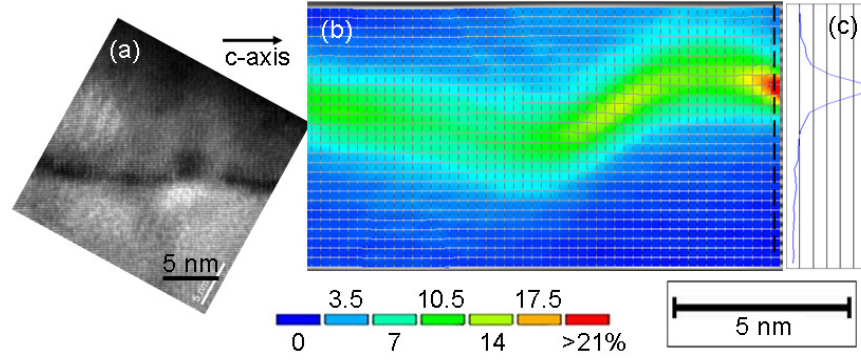
11

Fig. 8 Two-beam TEM image (a) and the corresponding SSA image (b) of a section of a sidewall QW near the middle height of the QW NR. Part (c) shows the line-scan indium content profile along the vertical dashed line in part (b).
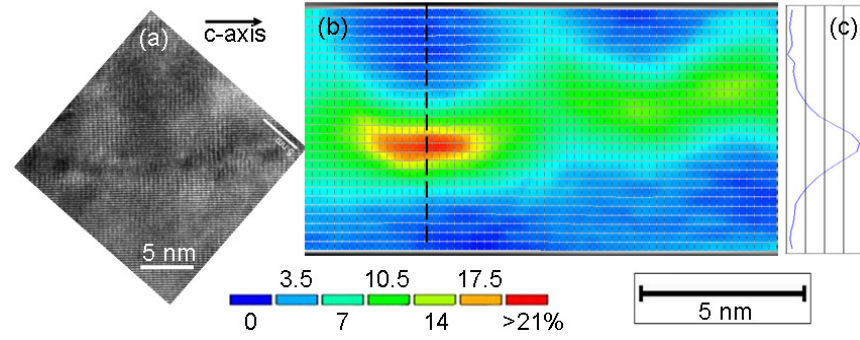

Fig. 9 Two-beam TEM image (a) and the corresponding SSA image (b) of a section of a sidewall QW near the bottom of the QW NR. Part (c) shows the line-scan indium content profile along the vertical dashed line in part (b).

Table II Average QW widths, indium contents, and their product values of the QWs at different locations.

	QW width (nm)	Indium content (%)	Product (nm %)
Top-face QW	4.72	12.72	60.04
Sidewall QW near the top	1.28	21.19	27.12
Sidewall QW near the middle height	1.56	19.20	29.95
Sidewall QW near the bottom	2.00	16.39	32.78

6. Discussions

In Fig. 3, we have demonstrated the local CL emission spectra at different locations of a QW NR. The CL spectrum with the peak wavelength around 450 nm in curve TF-c originates from the *c*-plane top-face QWs of 12.72 % in estimated indium composition and 4.72 nm in estimated QW width. Such an indium composition in such a wide QW, the emission wavelength can be somewhat longer. However, because of the lateral strain relaxation in these QWs, the reduced piezoelectric field can lead to a certain blue shift in emission spectrum [3], resulting in the emission around 450 nm. The used 5-kV electron accelerating voltage in the CL measurement can excite the sidewall QWs as deep as ~250 nm. Therefore, the spectrum labeled by

TF-r in Fig. 3 should consist of the major contributions from the top and middle-height portions of the sidewall QWs, i.e., the spectral curves of SW-t and SW-m. The trend of increasing estimated indium composition with height in the sidewall QWs is consistent with the trend of red-shifting spectral peak in Fig. 3. However, the significantly larger estimated indium compositions in the sidewall QWs, when compared with that of the top-face QWs, are expected to result in significantly longer emission wavelengths. Nevertheless, the spectral peak of curve SW-t is only around 460 nm. The spectral peak of curve SW-b is even shorter than 450 nm (around 448 nm). Such emission results are attributed to the following two factors. First, the estimated QW widths of the sidewall QWs are significantly smaller than that of the top-face QWs, leading to a much stronger quantum-confinement effect such that the emission spectrum is blue-shifted. Second, because of the non-polar nature of the sidewall QWs, the zero QCSE results in a shorter emission wavelength, when compared with a polar QW of the same indium composition [8, 9]. Therefore, the emission spectra of the sidewall QWs are all close to 450 nm. It is noted that the numerical estimations of the spectral blue-shift ranges due to the factors of stronger quantum confinement and zero QCSE are difficult because the emission behavior of such a QW is strongly affected by the structure of indium-rich nano-clustering (see Figs. 6-9) [39, 40].

In the fourth column of Table II, we show the product of the QW width and indium content in each QW category. These product values can be used for representing their total indium contents per unit surface area during the same growth period of a QW. Here, one can see that the top-face QWs have a significantly larger product value, when compared with those of the sidewall QWs. This product value decreases with the height on the sidewall. Such results can be interpreted as follows: Around an NR, the supplied constituent atoms (gallium, indium, which are formed through the decomposition of metalorganic precursors TEGa and TMIn, and nitrogen) projected onto the planar area of the NR cross section are mainly adsorbed by the top surface of the NR to form the top-face QW structure. Because of the abundant supply, the well and barrier layers of the QWs on the top face are quite thick, leading to the relatively lower indium composition in the QWs. Nevertheless, the total adsorbed indium content per unit surface area is still significantly higher than those on the sidewall. On the other hand, the constituent atoms projected onto the gaps between NRs flow down to the bottom of the gaps and migrate upward along the sidewall surfaces for forming the sidewall QW structures [41-44]. In this situation, the bottom portion of a sidewall can adsorb more constituent atoms than its top portion. Therefore, on the sidewall, the thicknesses of a GaN barrier layer and an InGaN well layer decrease with height. Also, the total adsorbed indium content per unit surface area decreases with height, as indicated by the product values in the fourth column of Table II. However, because of the smaller QW width near the top of the sidewall, the indium composition here becomes higher.

7. Conclusions

In summary, we have demonstrated the growth of a regularly-patterned, c-axis nitride NR array of uniform geometry with simultaneous depositions of c-plane disc-like and m-plane core-shell InGaN/GaN QW structures based on the nano-imprint lithography and the pulsed growth mode of MOCVD. The differences

of geometry and composition between these two groups of QW were studied with SEM, CL, and TEM. In particular, the SSA results provided us with the information about the QW width and composition. It was found that the QW widths were narrower and the indium contents were higher in the sidewall m-plane QWs, when compared with the top-face c-plane QWs. Also, in the sidewall QWs, the QW width (indium content) decreased (increased) with height. The observed results could be interpreted with the migration behavior of the constituent atoms along the NR sidewall from the bottom.

References:
1. Y. S. Chen, W. Y. Shiao, T. Y. Tang, W. M. Chang, C. H. Liao, C. H. Lin, K. C. Shen, C. C. Yang, M. C. Hsu, J. H. Yeh, and T. C. Hsu, "Threading dislocation evolution in patterned GaN nanocolumn growth and coalescence overgrowth," J. App. Phys. **106**, 023521 (2009).
2. R. Colby, Z. Liang, I. H. Wildeson, D. A. Ewoldt, T. D. Sands, R. E. Garcia, and E. A. Stach, "Dislocation filtering in GaN nanostructures," Nano Lett. **10**, 1568-1573 (2010).
3. H. S. Chen, D. M. Yeh, Y. C. Lu, C. Y. Chen, C. F. Huang, T. Y. Tang, C. C. Yang, C. S. Wu, and C. D. Chen, "Strain relaxation and quantum confinement in InGaN/GanN nanoposts," Nanotechnology **17**, 1454-1458 (2006).
4. C. Y. Wang, L. Y. Chen, C. P. Chen, Y. W. Cheng, M. Y. Ke, M. Y. Hsieh, H. M. Wu, L. H. Peng, and J. J. Huang, "GaN nanorod light emitting diode array with a nearly constant electroluminescent peak wavelength," Opt. Express **16**, 10549-10556 (2008).
5. C. F. Huang, T. Y. Tang, J. J. Huang, W. Y. Shiao, C. C. Yang, C. W. Hsu, and L. C. Chen, "Prestrained effect on the emission properties of InGaN/GaN quantum-well structures," Appl. Phys. Lett. **89**, 051913 (2006).
6. R. Koester, J. S. Hwang, D. Salomon, X. Chen, C. Bougerol, J. P. Barnes, D. L. S. Dang, L. Rigutti, A. De Luna Bugallo, G. Jacopin, M. Tchernycheva, C. Durand, and J. Eymery, "M-plane core-shell InGaN/GaN multiple-quantum-wells on GaN wires for electroluminescent devices," Nano Lett. **11**, 4839-4845 (2011).
7. Y. J. Hong, C. H. Lee, A. Yoon, M. Kim, H. K. Seong, H. J. Chung, C. Sone, Y. J. Park, and G. C. Yi, "Visible-color-tunable light-emitting diodes," Adv. Mat. **23**, 3284-3288 (2011).
8. M. D. Craven, P. Waltereit, J. S. Speck, and S. P. DenBaars, "Well-width dependence of photoluminescence emission from a-plane GaN/AlGaN multiple quantum wells," Appl. Phys. Lett. **84**, 496-498 (2004).
9. N. Fellows, H. Sato, H. Masui, S. P. Denbaars, and S. Nakamura, "Increased polarization ratio on semipolar (11-22) InGaN/GaN light-emitting diodes with increasing indium composition," Jpn. J. Appl. Phys. **47**, 7854-7856 (2008).
10. H. Sekiguchi, K. Kishino, and A. Kikuchi, "Emission color control from blue to red with nanocolumn diameter of InGaN/GaN nanocolumn arrays grown on same substrate," Appl. Phys. Lett. **96**, 231104 (2010).
11. W. Bergbauer, M. Strassburg, C. Kolper, N. Linder, C. Roder, J. Lahnemann, A. Trampert, S. Fundling, S. F. Li, H. H. Wehmann, and A. Waag, "Continuous-flux MOVPE growth of position-controlled N-face GaN nanorods and embedded InGaN quantum wells," Nanotechnology **21**, 305201 (2010).

12. Q. Li and G. T. Wang, "Spatial distribution of defect luminescence in GaN nanowires," Nano Lett. **10**, 1554-1158 (2010).
13. M. Y. Ke, C. Y. Wang, L. Y. Chen, H. H. Chen, H. L. Chiang, Y. W. Cheng, M. Y. Hsieh, C. P. Chen, and J. J. Huang, "Application of nanosphere lithography to LED surface texturing and to the fabrication of nanorod LED arrays," IEEE J. Sel. Top. Quantum Electron. **15**, 1242-1249 (2009).
14. T. Y. Tang, W. Y. Shiao, C. H. Lin, K. C. Shen, J. J. Huang, S. Y. Ting, T. C. Liu, C. C. Yang, C. L. Yao, J. H. Yeh, T. C. Hsu, W. C. Chen, and L. C. Chen, "Coalescence overgrowth of GaN nanocolumns on sapphire with patterned metal organic vapor phase epitaxy," J. Appl. Phys. **105**, 023501 (2009).
15. T. Y. Tang, W. Y. Shiao, Y. S. Chen, C. H. Lin, W. M. Chang, C. H. Liao, K. C. Shen, C. C. Yang, M. C. Hsu, J. H. Yeh, and T. C. Hsu, "Nitride nanocolumns for the development of light-emitting diode," IEEE Transact. Electron Dev. **57**, 71-78 (2010).
16. H. Lahrèche, P. Vennéguès, O.Tottereau, M. Laügt, P. Lorenzini, M. Leroux, B. Beaumont, and P. Gibart, "Optimisation of AlN and GaN growth by metalorganic vapour-phase epitaxy (MOVPE) on Si (1 1 1)," J. Crystal Growth **217**, 13-25 (2000).
17. L. W. Tu, C. L. Hsiao, T. W. Chi, I. Lo, and K. Y. Hsieh, "Self-assembled vertical GaN nanorods grown by molecular-beam epitaxy," Appl. Phys. Lett. **82**, 1601-1602 (2003).
18. C. Chèze, L. Geelhaar, B. Jenichen, and H. Riechert, "Different growth rates for catalyst-induced and self-induced GaN nanowires," Appl. Phys. Lett. **97**, 153105 (2010).
19. T. Song, W. I. Park, and U. Paik, "Epitaxial growth of one-dimensional GaN nanostructures with enhanced near-band edge emission by chemical vapor deposition," Appl. Phys. Lett. **96**, 011105 (2010).
20. X. J. Chen, G. Perillat-Merceroz, D. Sam-Giao, C. Durand, and J. Eymery, "Homoepitaxial growth of catalyst-free GaN wires on N-polar substrates," Appl. Phys. Lett. **97**, 151909 (2010)
21. Y. Kawakami, S. Suzuki, A. Kaneta, M. Funato, A. Kikuchi, and K. Kishino, "Origin of high oscillator strength in green-emitting InGaN/GaN nanocolumns," Appl. Phys. Lett. **89**, 163124 (2006).
22. K. Kishino, H. Sekiguchi, and A. Kikuchi, "Improved Ti-mask selective-area growth (SAG) by rf-plasma-assisted molecular beam epitaxy demonstrating extremely uniform GaN nanocolumn arrays," J. Crystal Growth **311**, 2063-2068 (2009).
23. S. D. Hersee, X. Sun, and X. Wang, "The controlled growth of GaN nanowires," Nano Lett. **6**, 1808-1811 (2006).
24. W. Guo, M. Zhang, A. Banerjee, and P. Bhattacharya, "Catalyst-free InGaN/GaN nanowire light emitting diodes grown on (001) silicon by molecular beam epitaxy," Nano Lett. **10**, 3355-3359 (2010).
25. W. Guo, A. Banerjee, P. Bhattacharya, and B. S. Ooi, "InGaN/GaN disk-in-nanowire white light emitting diodes on (001) silicon," Appl. Phys. Lett. **98**, 193102 (2011).
26. H. Lin, Y. Lu , H. Chen, H. Lee, and S. Gwo, "InGaN/GaN nanorod array white light-emitting diode," Appl. Phys. Lett. **97**, 073101 (2010).

27. K. Tachibana, T. Someya, S. Ishida, and Y. Arakawa, "Selective growth of InGaN quantum dot structures and their microphotoluminescence at room temperature," Appl. Phys. Lett. **76**, 3212-3214 (2000).

28. P. R. Edwards, R. W. Martin, I. M. Watson, C. Liu, R. A. Taylor, J. H. Rice, J. H. Na, J. W. Robinson, and J. D. Smith, "Quantum dot emission from site-controlled InGaN/GaN micropyramid arrays," Appl. Phys. Lett. **85**, 4281-4283 (2004).

29. X. Wang, X. Sun, M. Fairchild, and S. D. Hersee, "Fabrication of GaN nanowire arrays by confined epitaxy," Appl. Phys. Lett. **89**, 233115 (2006).

30. W. H. Goh, G. Patriarche, P. L. Bonanno, S. Gautier, T. Moudakir, M. Abid, G. Orsal, A. A. Sirenko, Z. H. Cai, A. Martinez, A. Ramdane, L. Le Gratiet, D. Troadec, A. Soltani, and A. Ougazzaden, "Structural and optical properties of nanodots, nanowires, and multi-quantum wells of III-nitride grown by MOVPE nano-selective area growth," J. Crystal Growth **315**, 160-163 (2011).

31. W. Bergbauer, M. Strassburg, C. Kolper, N. Linder, C. Roder, J. Lahnemann, A. Trampert, S. Fundling, S. F. Li, H.-H. Wehmann, and A. Waag, "N-face GaN nanorods: Continuous-flux MOVPE growth and morphological properties," J. Crystal Growth **315**, 164-167 (2011).

32. F. Qian, Y. Li, S. Gradecak, D. Wang, C. J. Barrelet, and C. M. Lieber, "Gallium nitride-based nanowire radial heterostructures for nanophotonics," Nano Lett. **4**, 1975-1979 (2004).

33. S. K. Lim, M. Brewster, F. Qian, Y. Li, C. M. Lieber, and S. Gradecak, "Direct correlation between structural and optical properties of III-V nitride nanowire heterostructures with nanoscale resolution," Nano Lett. **9**, 3940-3944 (2009).

34. A. De Luna Bugallo, L. Rigutti, G. Jacopin, F. H. Julien, C. Durand, X. J. Chen, D. Salomon, J. Eymery, and M. Tchernycheva, "Single-wire photodetectors based on InGaN/GaN radial quantum wells in GaN wires grown by catalyst-free metal-organic vapor phase epitaxy," Appl. Phys. Lett. **98**, 233107 (2011).

35. G. Jacopin, A. De Luna Bugallo, P. Lavenus, L. Rigutti, F. H. Jullien, L. F. Zagonel, M. Kociak, C. Durand, D. Salomon, X. J. Chen, J. Eymery, and M. Tchernycheva, "Single-wire light-emitting diodes based on GaN wires containing both polar and nonpolar InGaN/GaN quantum wells," Appl. Phys. Express **5**, 014101 (2012).

36. D. Gerthsen, B. Neubauer, A. Rosenauer, T. Stephan, H. Kalt, O. Schon, and M. Heuken, "Solid phase immiscibility in GaInN," Appl. Phys. Lett. **69**, 2701-2703 (1996).

37. D. Gerthsen, E. Hahn, B. Neubauer, V. Potin, A. Rosenauer, and M. Schowalter, "Indium distribution in epitaxially grown InGaN layers analyzed by transmission electron microscopy, " phys. stat. sol (c) **0**, 1668-1683 (2003).

38. Y. S. Chen, L. J. Yao, Y. L. Lin, L. Hung, C. F. Huang, T. Y. Tang, J. J. Huang, W. Y. Shiao, and C. C. Yang, "Transmission electron microscopy study on pre-strained InGaN/GaN quantum wells," J. Crystal Growth **297**, 66-73 (2006).

39. Y. S. Lin, K. J. Ma, C. Hsu, S. W. Feng, Y. C. Cheng, C. C. Liao, C. C. Yang, C. C. Chuo, C. M. Lee, and J. I. Chyi, "Dependence of composition fluctuation on indium content in InGaN/GaN multiple quantum wells," Appl. Phys. Lett. **77**, 2988-2990 (2000).

40. Y. C. Cheng, E. C. Lin, C. M. Wu, C. C. Yang, J. R. Yang, A. Rosenauer, K. J. Ma, S. C. Shi, L. C. Chen, C. C. Pan, and J. I. Chyi, "Nanostructures and carrier

localization behaviors of green-luminescence InGaN/GaN quantum-well structures of various silicon-doping conditions," Appl. Phys. Lett. **84**, 2506-2508 (2004).

41. R. K. Debnath, R. Meijers, T. Richter, T. Stoica, R. Calarco, and H. Luth, "Mechanism of molecular beam epitaxy growth of GaN nanowires on Si(111)," Appl. Phys. Lett. **90**, 123117 (2007).

42. J. Ristic, E. Calleja, S. Fernandez-Garrido, L. Cerutti, A. Trampert, U. Jahn, and K. H. Ploog, "On the mechanisms of spontaneous growth of III-nitride nanocolumns by plasma-assisted molecular beam epitaxy," J. Crystal Growth **310**, 4035-4045 (2008).

43. S. K. Lim, M. J. Tambe, M. M. Brewster, and S. Gradecak, "Controlled growth of ternary alloy nanowires using metalorganic chemical vapor deposition," Nano Lett. **8**, 1386-1392 (2008).

44. R. L. Woo, L. Gao, N. Goel, M. K. Hudait, and K. L. Wang, S. Kodambaka, and R. F. Hicks, "Kinetic control of self-catalyzed indium phosphide nanowires, nanocones, and nanopillars," Nano Lett. **9**, 2207-2211 (2009).

Part II:
n-GaN Grown on n-type 6H-SiC substrate with a Conducting Buffer Layer

Silicon carbide (SiC) substrate is suitable for the hetero-epitaxial growths of GaN-based high-power and high-temperature devices due to its high thermal conductivity (4.9 Wcm^{-1}/K) and small lattice mismatch with GaN (3.5%). Such conductive SiC substrate enables us to fabricate fully vertical conducting devices by forming an electrode on the backside of the substrate. For the growth of a high-quality GaN film on SiC substrate, an AlN buffer layer was widely used because of the small lattice mismatch (1%) from SiC and the similar thermal expansion coefficient. However, AlN is an insulator. Such a buffer layer cannot be used for the fabrication of a vertical conducting device on SiC substrate.

By using an MOCVD system, we can grow a composition-graded n-type $Al_xGa_{1-x}N$ layer on the n-type 6H-SiC substrate as a conducting buffer layer. The Al composition is linearly decreased from 20 to 0%. TMGa, TMAl and NH_3 are chosen as the sources of Ga, Al and N atoms, respectively. The TMAl flow rate is linearly decreased while the TMGa flow rate is linearly increased such that the total flow rate of alkyl source is maintained a constant. The doping level (with Si) of the buffer layer is $\sim 10^{18}/cm^3$. The growth temperature of the AlGaN buffer is 1000 ^{o}C and the growth chamber pressure is 76 torr, which is quite low for minimizing the homogeneous gas-phase reactions between TMAl and NH_3.

After the growth of the AlGaN buffer, a 1-μm n-type GaN layer is deposited at 1020 ^{o}C intemperature and 200 torr in chamber pressure with a deposition rate of 2 μm/h. The doping level is also $\sim 10^{18}/cm^3$. Then we use a Ti/Au (50 nm/150 nm) layered metal structure and an indium ball as the n-SiC and n-GaN metal contacts, respectively, for measuring the electrical property of the sample. The sample structures without and with metal contacts are shown in Figs. 10 and 11, respectively.
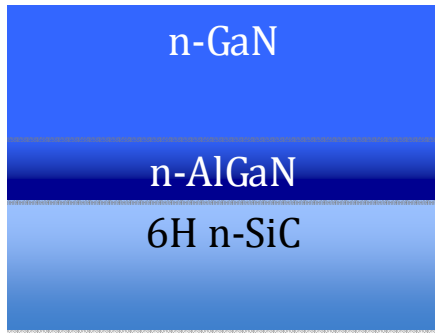

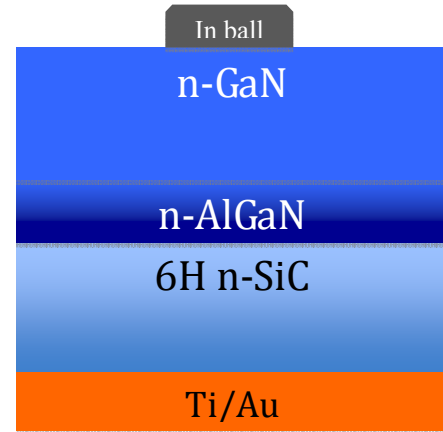Fig. 10 sample structure without metal contacts.   Fig. 11 sample structure with metal contacts.

For optimizing the growth conditions, we prepare four samples with different growth conditions and compare their electrical properties. Their growth conditions and measurement results are shown in Table III.

Table III Growth conditions and electrical properties of the four samples.

Sample	Growth Pressure of AlGaN (torr)	Initial Al Composition (%)	Thickness of AlGaN (nm)	Vertical Resistance (Ω)
A	200	20	50	2400
B	76	20	50	800
C	76	20	150	64
D	76	20	250	120

From the comparison between the four samples shown in Table III, one can see that the growth pressure of AlGaN should be lower 100 torr for enhancing the Al incorporation efficiency and the crystal quality. When the thickness of AlGaN is 50 nm (sample B), the epitaxial layer is cracked due to the induced tensile stress during the sample cooling process. To solve this problem, we increase the thickness of AlGaN to 150 nm in sample C. In this sample, the cracking behavior is significantly reduced. However, cracking can still be observed, as shown in the plan-view SEM images of sample C (see Figs. 12 and 13). In particular, the cracking behavior is stronger around a pit, as shown in Fig. 13. At this moment, the cause for the pit (threading dislocation beneath or other crystal defect) is still unclear.
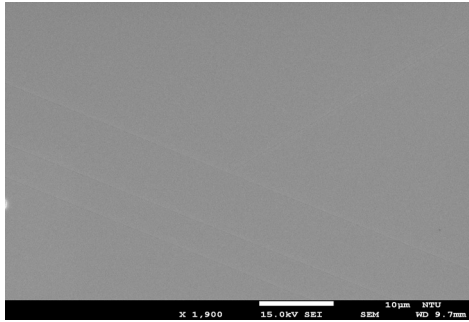

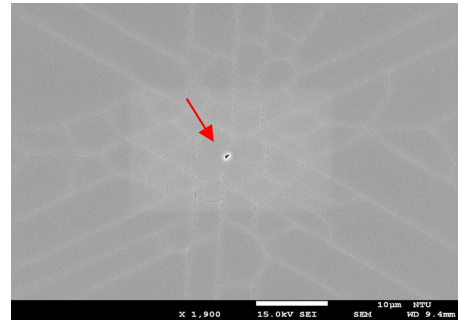Fig. 12 A plan-view SEM image of sample C.   Fig. 13 Another plan-view SEM image of sample C.

To see whether we can completely delete the cracking behavior, we further increase the thickness of AlGaN to 250 nm in sample D. Unfortunately, the cracking behavior in sample D is about the same as that of sample C. Even worse, the vertical resistance in sample D is increased from 64 to 120 Ω. Therefore, except the cracking issue, sample C represents the optimized growth condition in minimizing the vertical resistance. The I-V curve of sample C is shown in Fig. 14. Also, the ω-relative scan result of X-ray diffraction (XRD) of sample C is shown in Fig. 15. The full-width at half-maximum (FWHM) of the scan pattern of n-GaN is 291.5 arcsec, indicating the high crystal quality of the grown n-GaN layer. The atomic force microscopy (AFM) image of sample C is shown in Fig. 16. Here, one can see nano-scale droplets on the surface. So far, we have not figured out the composition of those nano-droplets yet. However, they can be either Ga or Al. With those nano-droplets, the rms roughness of the surface of sample C is 5.86 nm.
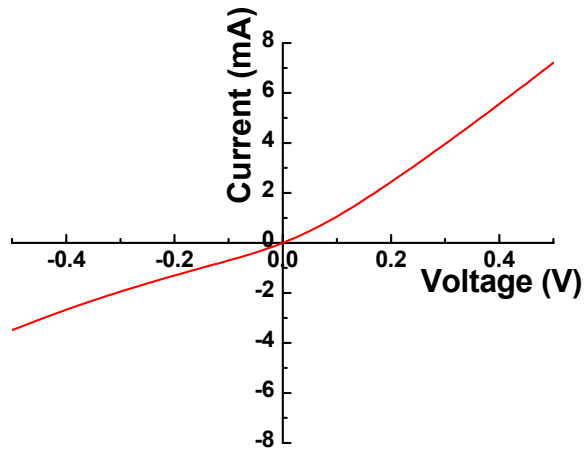
Fig. 14 I-V curve of sample C.

In summary, we have demonstrated the growth of a conducting nitride layer of low vertical resistance (64 Ω) on 6H n-type SiC substrate. The nitride layer consisted of a 150-nm n-AlGaN layer with the Al composition being linearly decreased from 20 to 0% and a 1-µm n-GaN layer. Both layers were Si doped with a level around 10^{18}/cm^3. The growth condition of the n-AlGaN layer must be further improved to obtain a crack-free and smooth surface.
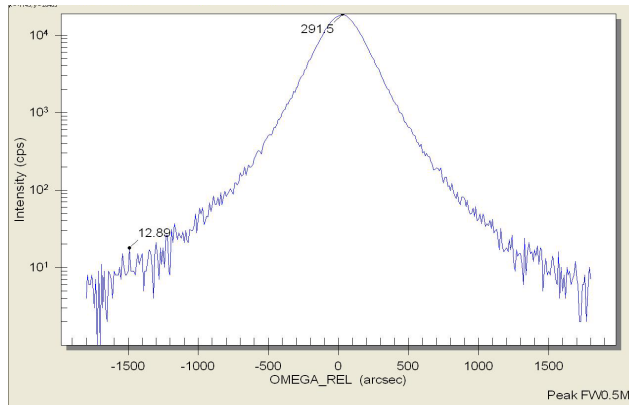

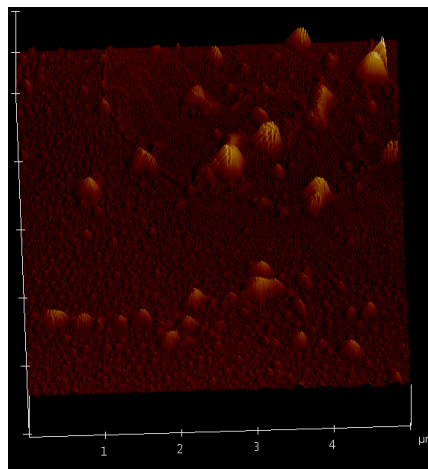Fig. 15 ω-relative scan result of XRD of sample C.

Fig. 16 AFM image of sample C.

20

Part III:
Related Journal Publication List (acknowledging AOARD)

1. Shao-Ying Ting, Yu-Feng Yao, Wei-Lun Chung, Wen-Ming Chang, Chih-Yen Chen, Hao-Tsung Chen, Che-Hao Liao, Horng-Shyang Chen, Chieh Hsieh, and <u>C. C. Yang</u>, "Comparison of Emission Characteristics between the CdZnO/ZnO Quantum Wells on ZnO and GaN Templates," accepted for publication in Optics Express.
2. Chieh Hsieh, Horng-Shyang Chen, Che-Hao Liao, Chih-Yen Chen, Chun-Han Lin, Cheng-Hung Lin, Shao-Ying Ting, Yu-Feng Yao, Hao-Tsung Chen, Yean-Woei Kiang, and <u>C. C. Yang</u>, "Photoelectrochemical Liftoff of Patterned Sapphire Substrate for Fabricating Vertical Light-emitting Diode," accepted for publication in IEEE Photonics Technology Letters.
3. Chih-Yen Chen, Wen-Ming Chang, Wei-Lun Chung, Chieh Hsieh, Che-Hao Liao, Shao-Ying Ting, Kuan-Yu Chen, Yean-Woei Kiang, <u>C. C. Yang</u>, Wei-Siang Su, and Yung-Chen Cheng, "Crack-free GaN deposition on Si substrate with temperature-graded AlN buffer growth and the emission characteristics of overgrown InGaN/GaN quantum wells," to appear in Journal of Crystal Growth.
4. Wen-Ming Chang, Che-Hao Liao, Chih-Yen Chen, Chieh Hsieh, Tsung-Yi Tang, Yean-Woei Kiang, and <u>C. C. Yang</u>, "Spiral deposition with alternating indium composition in growing an InGaN nano-needle with the vapor-liquid-solid growth mode," Journal of Nanomaterials, vol. 2012, Article ID 653195, 7 pages, 2012. doi:10.1155/2012/653195.
5. Che-Hao Liao, Wen-Ming Chang, Chih-Yen Chen, Yu-Feng Yao, Hao-Tsung Chen, Horng-Shyang Chen, Chia-Ying Su, Shao-Ying Ting, Dong-Ming Yeh, Yean-Woei Kiang, and <u>C. C. Yang</u>, "Geometry and composition comparisons between c-plane disc-like and m-plane core-shell InGaN/GaN quantum wells in a nitride nanorod," Optics Express, Vol. 20, Issue 14, pp. 15859-15871 July 2, (2012).
6. Shao-Ying Ting, Horng-Shyang Chen, Wen-Ming Chang, Jeng-Jie Huang, Che-Hao Liao, Chih-Yen Chen, Chieh Hsieh, Yu-Feng Yao, Hao-Tsung Chen, Yean-Woei Kiang, and <u>C. C. Yang</u>, "MBE-grown CdZnO/ZnO Multiple Quantum-well Light-emitting Diode on MOCVD-grown p-type GaN," IEEE Photonics Technology Letters, Vol. 24, No. 11, p. 909~911, 1 June 2012.
7. Chih-Yen Chen, Chieh Hsieh, Che-Hao Liao, Wei-Lun Chung, Hao-Tsung Chen, Wenyu Cao, Wen-Ming Chang, Horng-Shyang Chen, Yu-Feng Yao, Shao-Ying Ting, Yean-Woei Kiang, <u>C. C. Yang</u>, and Xiaodong Hu, "Effects of overgrown p-layer on the emission characteristics of the InGaN/GaN quantum wells in a high-indium light-emitting diode," Optics Express, Vol. 20, No. 10, p. 11321~11335, 7 May 2012.
8. Hung-Yu Lin, Yang Kuo, Cheng-Yuan Liao, <u>C. C. Yang</u>, and Yean-Woei Kiang, "Surface plasmon effects in the absorption enhancements of amorphous silicon solar cells with periodical metal nanowall and nanopillar structures," Optics Express, Vol. 20, No. S1, p. A104~A118, 2 January 2012.
9. Che-Hao Liao, Chih-Yen Chen, Horng-Shiang Chen, Kuang-Yu Chen, Wei-Lun Chung, Wen-Ming Chang, Jeng-Jie Huang, Yu-Feng Yao, Yean-Woei Kiang, and <u>C. C. Yang</u>, "Emission efficiency dependence on the overgrown p-GaN thickness

in a high-indium InGaN/GaN quantum-well light-emitting diode," IEEE Photonics Technology Letters, Vol. 23, No. 23, p. 1757~1759, 1 December 2011.

10. Che-Wei Huang, Hung-Yu Tseng, Chih-Yen Chen, Che-Hao Liao, Chieh Hsieh, Kuan-Yu Chen, Hung-Yu Lin, Horng-Shyang Chen, Yu-Lung Jung, Yean-Woei Kiang, and C. C. Yang, "Fabrication of surface metal nanoparticles and their induced surface plasmon coupling with subsurface InGaN/GaN wells," Nanotechnology, Vol. 22, No. 47, p. 475201-1~8, 25 November 2011.

11. Shou-Yen Wu, Wen-Ming Chang, Hung-Yu Tseng, Cheng-Kuang Lee, Ting-Ta Chi, Jyh-Yang Wang, Yean-Woei Kiang, and C. C. Yang, "Geometry for Maximizing Localized Surface Plasmon Resonance of Au Nanorings with Random Orientations," Plasmonics, Vol. 6, No. 3, p. 547~555, September 2011.